Journal of Polymer Science and Engineering 2025, 8(1), 11589.
https://doi.org/10.24294/jpse11589

Article

Dependence of the magnetite (Fe_3O_4) and silica (SiO_2) nanostructured heterojunction for the photodegradation of tartrazine yellow dye

Marccus Victor Almeida Martins[1,*], Nathália Sayuri Tateno[2], Paulo Vitor Ribeiro Brito[2], Jocélia Pereira de Carvalho Oliveira[2]

[1] Coordenação de Cursos, Campus Catalão, Instituto Federal Goiano, Catalão-Goiás 75701-655, Brazil
[2] Instituto de Química, Universidade Federal de Catalão, Catalão-Goiás 75705-220, Brazil
*** Corresponding author:** Marccus Victor Almeida Martins, marccus.victor@ifgoiano.edu.br

CITATION

Martins MVA, Tateno NS, Brito PVR, Oliveira JPdC. Dependence of the magnetite (Fe_3O_4) and silica (SiO_2) nanostructured heterojunction for the photodegradation of tartrazine yellow dye. Journal of Polymer Science and Engineering. 2025; 8(1): 11589.
https://doi.org/10.24294/jpse11589

ARTICLE INFO

Received: 7 March 2025
Accepted: 3 April 2025
Available online: 8 April 2025

Abstract: This work investigated the photocatalytic properties of polymorphic nanostructures based on silica (SiO_2) and magnetite (Fe_3O_4) for the photodegradation of tartrazine yellow dye. In this sense, a fast, easy, and cheap synthesis route was proposed that used sugarcane bagasse biomass as a precursor material for silica. The Fourier transform infrared (FTIR) spectroscopy results showed a decrease in organic content due to the chemical treatment with NaOH solution. This was confirmed through the changes promoted in the bonds of chromophores belonging to lignin, cellulose, and hemicellulose. This treated biomass was calcined at 800 °C, and FTIR and X-ray diffraction (XRD) also confirmed the biomass ash profile. The FTIR spectrum showed the formation of silica through stretching of the chemical bonds of the silicate group (Si-O-Si), which was confirmed by DXR with the predominance of peaks associated with the quartz phase. Scanning electron microscopy (SEM) and energy dispersive X-ray spectroscopy (EDS) confirmed the morphological and chemical changes due to the chemical and thermal treatments applied to this biomass. Using the coprecipitation method, we synthesized Fe_3O_4 nanoparticles (Np) in the presence of SiO_2, generating the material Fe_3O_4/SiO_2-Np. The result was the formation of nanostructures with cubic, spherical, and octahedral geometries with a size of 200 nm. The SEM images showed that the few heterojunctions formed in the mixed material increased the photocatalytic efficiency of the photodegradation of tartrazine yellow dye by more than two times. The degradation percentage reached 45% in 120 min of reaction time. This mixed material can effectively decontaminate effluents composed of organic pollutants containing azo groups.

Keywords: decontamination; organic pollutants; photocatalyze; sugarcane; magnetite nanoparticles; coprecipitation

1. Introduction

The development of technologies [1] for effluent decontamination has been growing due to the increase in industrial processes [2] since industrial products contaminate the environment, causing enormous damage to humanity. Advanced Oxidation Processes (AOPs) [3] bring advantages, such as efficiency in oxidizing these pollutants, while not generating secondary products. Different configurations of photocatalyst materials based on metals and metal oxides have been widely investigated in the literature to improve AOPs [2,4,5]. Important aspects for efficient photodegradation of pollutants, such as physicochemical and morphological properties, are highlighted within these nano- and microstructured photocatalysts. Considering the separation between the valence band (VB) and conduction band (CB), a favorable band gap to inhibit recombination between the holes (h^+) generated in the

VB and the photogenerated electrons (e^-) in the CB of the semiconductor plays a crucial role. Recombination is more strongly favored in semiconductors with band gap values above 3.0 eV [6], making the photodegradation of pollutants difficult. Therefore, ensuring a high quantity of positive and negative charges in the semiconductor generates a greater quantity of radicals due to the attack of these charges on molecules in the medium, such as H_2O and O_2.

Textile and food dyes constitute a significant category of pollutants that cause damage to the environment when present in an inappropriate form. These organic molecules have a high molecular mass and generally do not undergo natural degradation in the environment. Since dyes are molecules rich in electrons, in the presence of $HO^{\bullet}$ and $O_2^{\bullet -}$ radicals, they tend to undergo degradation reactions, reducing into smaller molecules that can degrade more easily in the environment.

Several studies [7] have widely investigated the intrinsic modification of oxides (doping) consisting of metals belonging to groups II to IV to decrease the energy required to promote electrons, facilitating the formation of h^+/e^- charges that will generate radicals to react with polluting organic molecules. In contrast, the formation of heterojunctions [8,9] in the structures of materials based on metal oxides is also a strategy reported in studies on inhibiting charge recombination in the semiconductor. Ashiegbu and Potgieter [10] demonstrated that the formation of heterojunctions in the composite consisting of zinc oxide and tungstate was decisive for the rapid photodegradation of the methyl orange dye. In the same sense, Shahazad et al. [11] also proved that the formation of heterojunctions in the nanomaterial consisting of silver and titanium oxide increased the lifetime of the charges generated in the catalyst, enhancing the photodegradation reaction of the methylene blue and methyl orange dyes. When analyzing all these works, it is evident that the synergy caused by the formation of a heterojunction is crucial in the photocatalytic performance in the degradation of dyes.

Titanium oxide (TiO_2) is commonly used to treat specific nanoparticles in photodegradation. However, it presents some disadvantages, such as the high cost of the ionic precursor, the time-consuming synthesis routes, and the limited use in the visible spectrum [12]. In contrast, magnetite nanoparticles (Fe_3O_4) [13] have also become widely used in effluent decontamination. This is mainly due to the low cost of the precursor salts, the rapid and simple synthesis routes, the ability to control physicochemical and morphological properties, and the reuse of the photocatalyst through external magnetic collection. Jaehun et al. [14] developed a composite material consisting of graphene oxide, tungstate, and magnetite for the photocatalysis of malachite green dye and chromium ions. The synthesized material generated the formation of heterojunctions that enhanced the photodegradation of the dye and chromium ion.

From the point of view of magnetite synthesis, the literature [15] presents several routes for obtaining it. However, synthesis through the coprecipitation method stands out from the others due to the ease with which magnetic nanoparticles are formed in an aquatic environment. Factors such as room temperature, speed of selection of iron ions in a basic medium, and control of particle size are factors that make this route widely used for the synthesis of this material.

Thus, this work proposed the synthesis of a mixed material based on SiO_2 and Fe_3O_4 for the photocatalytic degradation of tartrazine yellow dye. We obtained photocatalyst material by combining low-cost materials, biomass reuse from sugarcane bagasse, and rapid synthesis. We analyzed the morphological and physicochemical properties of the Fe_3O_4/SiO_2-Np to understand the photodegradation mechanism of the tartrazine yellow dye (-N = N-) in an aqueous medium. In this regard, this work focused on the proposal of a low-cost material with the reuse of a biomass that is often discarded irregularly to serve as a support in the synthesis of magnetite. This easy and fast synthesis of the Fe_3O_4/SiO_2 nanocomposite meets the objective of a versatile and efficient material in the degradation of organic dyes, compared to other materials that present complex, expensive, and time-consuming configurations to obtain for the same purpose.

2. Materials and methods

2.1. Obtaining silica (SiO_2)

Figure 1a shows the sugarcane bagasse biomass collected from a street market located in the city center of Catalão, Goiás, Brazil. The biomass was washed with distilled water to remove impurities and small insects. Then, it was cut into small pieces and placed in an oven at 80 ℃ for 24 h to remove excess water. Finally, it was crushed in a blender to obtain particulate material, as shown in **Figure 1b**. This pulverized material underwent chemical treatment with an NaOH solution (1.0 mol L^{-1}) for 1 h. Then, it was washed with distilled water until the wash water reached a neutral pH (pH = 7). After the treated and washed biomass was completely dried, it was burned in a muffle furnace at 800 ℃ at a heating rate of 10 ℃/min for 1 h to obtain biomass ash, as presented in **Figure 1c**.

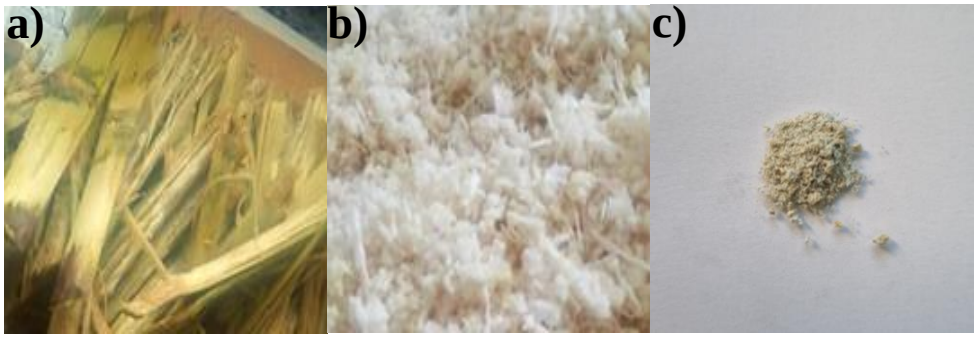

Figure 1. (a) Photographs showing the sugarcane bagasse biomass; **(b)** washed and pulverized biomass; **(c)** biomass ash.

2.2. Synthesis of the Fe_3O_4/SiO_2 nanoparticles

The synthesis of Fe_3O_4/SiO_2 nanoparticles used analytical grade reagents without further purification. Ferric chloride ($FeCl_3$), ferrous chloride ($FeCl_2$), and ammonium hydroxide (NH_4OH) were purchased from Aldrich. Fe_3O_4/SiO_2-Np was synthesized by the coprecipitation method [16] with some modifications. First, the solutions were prepared using distilled water: 25 mL of $FeCl_2$ (1 mmol L^{-1}) and 50 mL of $FeCl_3$ (1 mmol L^{-1}). In a three-necked glass flask, 25 mL of $FeCl_2$ and 50 mL of $FeCl_3$ were

added under constant stirring, with a controlled atmosphere (N_2 gas), at 50 °C. Then, 150 μL of NH_4OH (7 mol L^{-1}) were added. Instantly, 50 mL of SiO_2 suspension (0.1 g L^{-1}) were added, followed by another 150 μL of NH_4OH. The system was turned off minutes after the solution had changed from yellow to black. After the addition of 150 μL of NH_4OH to the solution, an abrupt change from yellow to black occurred, typical of magnetite. The addition of another 150 μL was necessary to ensure a complete supply of iron ions. This entire synthesis procedure lasted only 5 min.

2.3. Photodegradation of tartrazine yellow dye

For photocatalytic degradation, a 50 ppm stock solution of tartrazine yellow dye was prepared in double distilled water. Photodegradation experiments were carried out with a solution of 50 ppm of tartrazine yellow dye. First, 0.5 g L^{-1} of Fe_3O_4/SiO_2-Np was directly added to 100 mL of tartrazine yellow dye solution and placed in a photo-reactor. Then, the mixture was placed under magnetic stirring and subjected to the UV irradiation from a mercury vapor lamp of 125 W. The mixture was stirred for 1 h in the absence of light to promote the adsorption of tartrazine yellow dye on the photocatalyst (which was considered as time 0 in all graphs). After 1 h, the reactor lamp was turned on, and the reaction was conducted for 120 min. At 15-minute intervals, 3 mL of the solution was collected and analyzed using a UV-Vis spectrophotometer at a maximum wavelength of 426 nm, which corresponds to the maximum absorbance of the azo group of tartrazine. For each aliquot removed, an external magnetic field was applied to separate Fe_3O_4/SiO_2-Np from the solution.

2.4. Characterizations of Fe_3O_4/SiO_2-Np

UV-Vis spectroscopy experiments were performed in a Varian spectrophotometer at 25 °C, ranging from 200 to 800 nm, using a 1 cm long quartz cuvette. The morphology and size of Fe_3O_4/SiO_2-Np were analyzed in a field emission gun scanning electron microscope (FEG-SEM) Jeol Brand, JSM-7100FT, using the secondary electrons. For the FEG-SEM analysis, a small amount of Fe_3O_4/SiO_2-Np was dripped on carbon tape. Chemical mapping was performed by energy dispersive X-ray spectroscopy (EDS) coupled to FEG-SEM. The X-ray diffraction (XRD) analyses were performed on a Shimadzu XRD-6100 diffractometer operated at 30 kV and 30 mA and equipped with Cu-Kα radiation and a graphite monochromator in a range from 5° to 85°. The Fourier transform infrared (FTIR) spectroscopy analysis was carried out in a Cary 630 FTIR Spectrometer (Agilent) in attenuated total reflectance (ATR) mode, with a wavelength range between 4000 and 500 cm^{-1} and resolution of 4 cm^{-1}.

3. Results and discussion

3.1. Production of SiO_2 from sugarcane bagasse biomass

The sugarcane bagasse biomass, after being washed and powdered, was initially treated in a basic medium in an NaOH solution (0.1 mol L^{-1}). After this chemical treatment, the natural biomass color slightly changed from a whitish color (**Figure 2a**) to a slightly pinkish color (**Figure 2b**). This slight color change is associated with the

reaction between the hydroxyl ions (HO^-) and the lignocellulosic biomass units [17,18]. **Figure 2c** shows the FTIR spectra to highlight this reaction. The FTIR spectra for natural biomass (black line) and biomass treated with NaOH (0.1 mol L^{-1}) (red line) indicated vibrational stretching modes [19,20] associated with O-H, C-H, C=O, and C-O bonds, respectively, at 3400, 2899, 1718, and 1240 cm^{-1}. We can also observe a vibrational mode corresponding to the angular deformation of the C-O-C group at 1039 cm^{-1}. Most of these vibrational modes appeared with lower peak intensity and shifted to lower wavenumbers. This demonstrates that the basic medium tends to reduce the organic content as the HO^- ions react with the lignocellulosic biomass units, as reported in other studies [21,22]. Reducing this organic content in this pre-treatment is important to reduce the biomass calcination time, facilitating the conversion to ash.

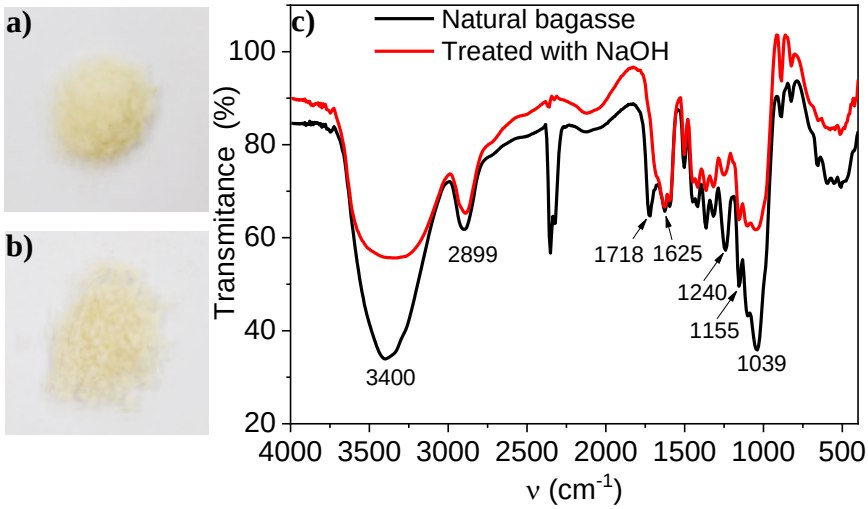

Figure 2. (a) Photographs of natural biomass; **(b)** biomass treated with NaOH (0.1 mol L^{-1}); **(c)** Fourier transform infrared (FTIR) spectra for natural biomass (black line) and biomass treated with NaOH (0.1 mol L^{-1}) (red line).

When the biomass treated in a basic medium was subjected to heat treatment at a temperature of 800 °C, for one hour in the muffle furnace, the material changed its color to a grayish tone, typical of products arising from the combustion of organic matter. **Figure 3** shows the SEM images to detail this morphology and to analyze this change from organic to inorganic matter. Typical plant structures, such as fibers (**Figure 3a**) and plant cells with hexagonal geometry (**Figure 3b**), are clearly visible and highlighted in red in natural biomass [23]. **Figure 3c**,**d** show that these fibrous and cell structures disappeared completely, followed by the presence of micropores [24] in the biomass sample calcined for 1 h at 800 °C. These characteristics demonstrate the formation of ash with a shapeless and randomly spread particle profile [25].

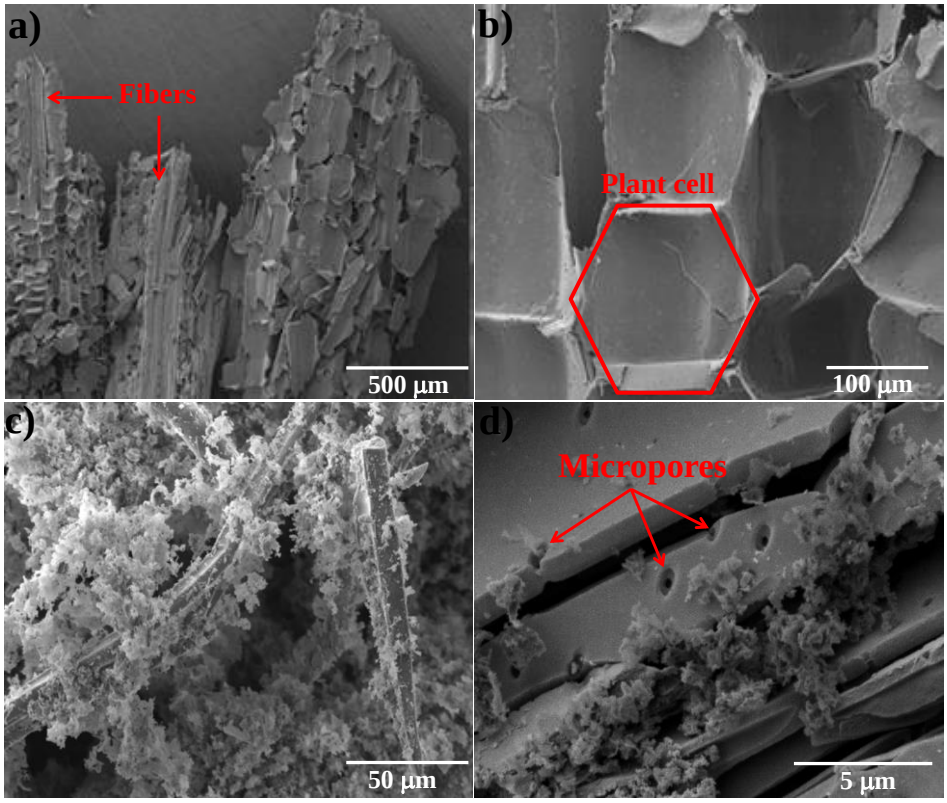

Figure 3. (a) Scanning electron microscopy (SEM) images for natural biomass with 50× magnification; **(b)** with 500× magnification; **(c)** scanning electron microscopy (SEM) images for biomass ash with 500× magnification; **(d)** and with 3000× magnification.

X-ray diffractometry was used to obtain information on the crystallographic behavior of the ash and natural fiber. In this sense, the diffractogram in **Figure 4a** was performed with angles ranging from 10 to 75 degrees, where the main peaks that represent the crystallographic phases of the silica present in the ash are indexed. The peaks located at approximately 2θ = 21.88°, 32.32°, 36.44°, 37.84°, 45.04°, 48.60°, and 57.28° can be attributed to crystalline SiO_2 (quartz) [26]. In contrast, **Figure 4b** shows that the natural biomass is an amorphous material [25]. The peaks at 2θ = 16° and 22° indicate a certain crystallinity of the cellulose [27,28]. In **Figure 4c**, the EDS results also confirmed the basic composition of the biomass ash, which presents oxygen and silicon with high energy and other metals, such as potassium, sodium, and magnesium, with low energy.

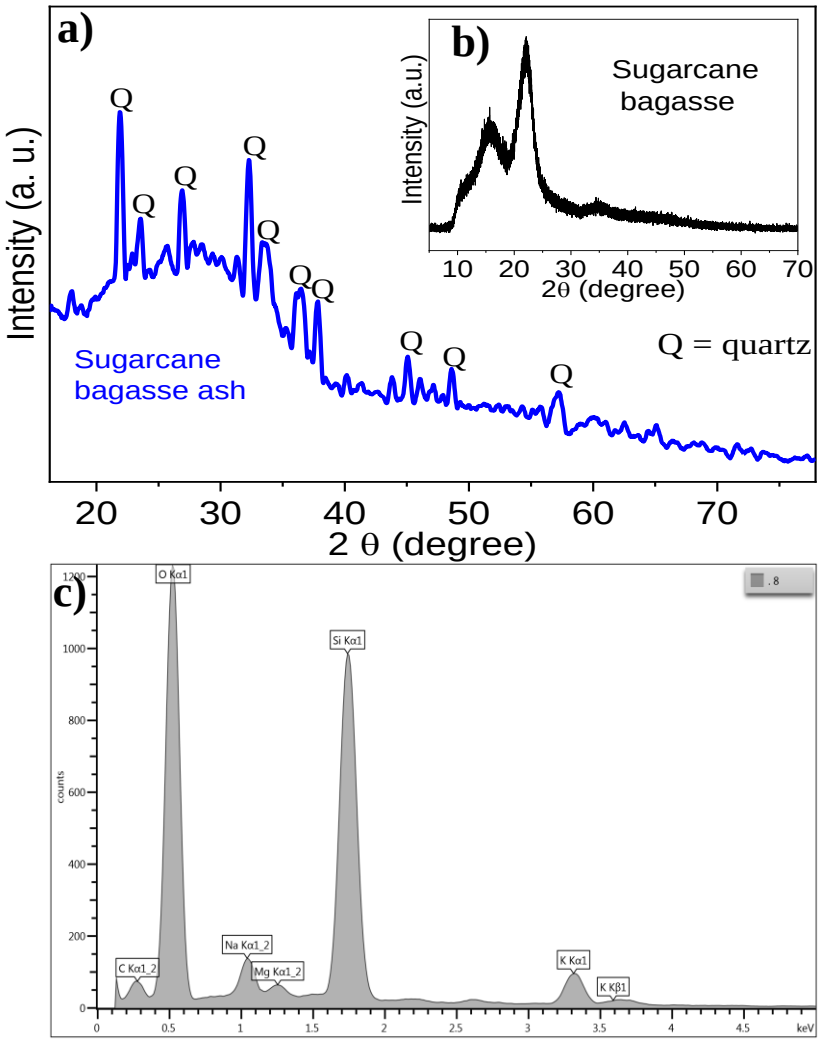

Figure 4. (a) X-ray diffraction (XRD) patterns for biomass ash; **(b)** natural biomass; **(c)** chemical mapping performed by energy dispersive X-ray spectroscopy (EDS).

3.2. Synthesis of Fe_3O_4/SiO_2 nanoparticles

The synthesis of magnetic iron oxide nanoparticles (Fe_3O_4-Np) was carried out based on the coprecipitation method [16] in the presence of SiO_2 and NH_4OH, as detailed in part 2 of Section 2. **Figure 5a** shows a sequence of photographs after the synthesis and the qualitative test of external magnetization applied to the material suspension. In this image, the dark brown coloration and the response of the material in the direction of the applied external magnetic field can be noted. These characteristics suggest the successful formation of Fe_3O_4 [16,29]. UV-Vis spectroscopy and XRD analysis confirmed the formation of Fe_3O_4. **Figure 5b** shows the behavior of the Fe_3O_4/SiO_2-Np, represented by the red line spectrum. The studied range showed typical no absorption bands, but an elevation in the baseline is a typical characteristic of Fe_3O_4 in aqueous suspension [16,30]. There were not absorption bands associated only with SiO_2 (blue spectrum). In **Figure 5c**, the UV-Vis absorption spectra enabled us to estimate the band gap between SiO_2 and Fe_3O_4/SiO_2-Np materials. Considering the Tauc plot $(\alpha h\nu \times E)^n$ [31], where α is the absorption coefficient, h is Planck's constant, ν is the photon frequency, n is equal to 2 (direct

transitions), and *E* is the energy in eV, and extrapolating the tangent line to the curves, we obtained the band gap energy of 2.65 eV and 2.35 eV for SiO_2 and Fe_3O_4/SiO_2-Np, respectively. The decrease of 0.3 eV for the Fe_3O_4/SiO_2-Np can be explained by the formation of a heterojunction generated in the mixed composite [32]. The XRD diffractogram in **Figure 5d**, for the Fe_3O_4/SiO_2-Np, showed high intensity and narrow-based peaks at 2θ = 23° (111), 31° (220), 32° (311), 47° (400), 52° (422), and 58° (511), which correspond to Fe_3O_4 [33]. Broadness of diffraction peaks indicates the nano-crystalline nature of the sample [34]. There were no crystallographic peaks associated with SiO_2 (see **Figure 4a**). This can be explained by the greater mass generated by Fe_3O_4 nanoparticles superimposed on the SiO_2 surface.

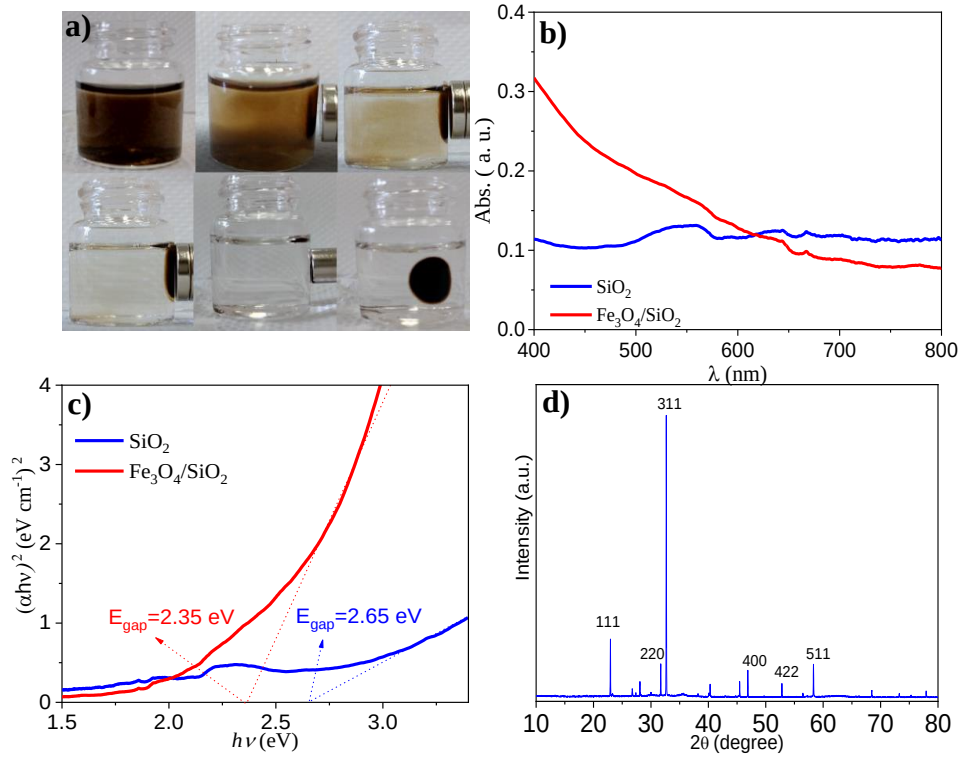

Figure 5. (a) Photographs showing the qualitative test of Fe_3O_4 with a neodymium magnet; **(b)** UV-Vis spectra for SiO_2 (blue) and Fe_3O_4/SiO_2-Np (red); **(c)**Tauc plot for obtaining the band gap energy of SiO_2 (blue) and Fe_3O_4/SiO_2-Np (red); **(d)** XRD diffractogram for Fe_3O_4/SiO_2-Np.

Figure 6 presents the SEM and EDS results for Fe_3O_4/SiO_2-Np to better understand how Fe_3O_4 formation occurred in the presence of SiO_2. **Figure 6a** shows structures with distinct geometries and dimensions with smaller particles with approximately spherical geometry agglomerated and larger particles with approximately cubic geometry. **Figure 6b,c** show the EDS spectra when performing the chemical mapping at points 1 and 5, highlighted by the red circle, exactly in the two distinct geometric profiles. Interestingly, the chemical constitution at these points converges to SiO_2 in the particles with cubic geometry (point 1) and other metal oxides (point 5), mainly Fe_3O_4. **Figure 6d** shows octahedral geometry shapes when scanning other points of the material and increasing the resolution. This geometrical polymorphism in the Fe_3O_4/SiO_2-Np (spherical, cubic, octahedral) completely agrees

with the XRD diffractogram in **Figure 5d**. The Fe_3O_4 particles (smaller) have a larger surface area and represent, to a greater extent, the X-ray reflections when compared to the SiO_2 reflections, which practically disappeared in this diffractogram. Analyzing these images and others, the average diameter obtained from the spherical particles was 200 nm for Fe_3O_4. In contrast, the dimensions of larger particles with cubic geometries have an edge with a length of 1.5 μm.

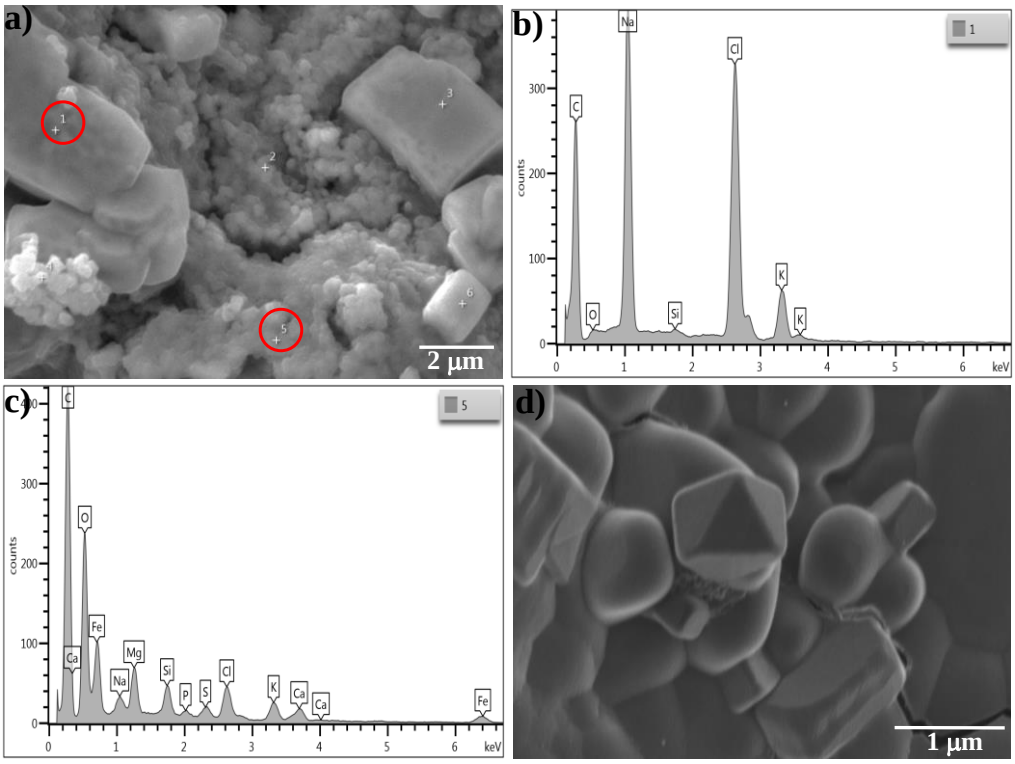

Figure 6. (a) Scanning electron microscopy (SEM) image highlighting the location of the chemical mapping points performed by energy dispersive X-ray spectroscopy (EDS) with red circles (points 1 and 5); **(b)** and **(c)** energy dispersive X-ray spectroscopy (EDS) spectra for points 1 and 5; **(d)** scanning electron microcopy (SEM) image of Fe_3O_4 polymorphic nanostructures at 20,000 x magnification.

By analyzing the SEM images associated with the XRD and EDS results, we can propose a mechanism for the formation of polymorphic nanostructures. After adding 150 μL of NH_4OH to the solution containing Fe^{2+} and Fe^{3+} ions, precipitation occurred, followed by a decrease in the oxidation states of the iron ions. This process is developed by the mass nucleation and agglomeration between nanoparticles with approximately spherical geometry. With excess NH_4OH (by adding another 150 μL) and SiO_2 particles, the nucleation process of additional iron ions occurs, forming spherical particles deposited on the surface of SiO_2 microparticles. Interestingly, other nucleation and growth processes of nanoparticles occur in the absence of SiO_2 and generate other geometric shapes, such as cubic and octahedral geometries. **Figure 7** presents the mechanism proposed for this synthesis.

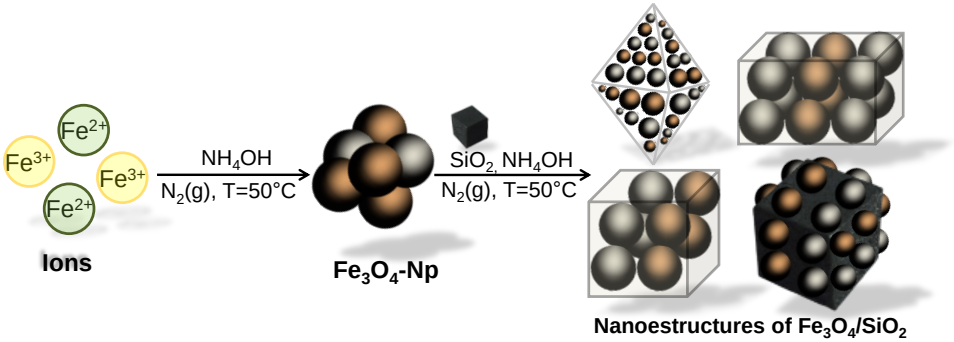

Figure 7. Schematic representation of the synthesis process of SiO_2 and Fe_3O_4 nanostructures.

3.3. Photodegradation of tartrazine yellow dye

The photocatalytic properties of SiO_2 and Fe_3O_4/SiO_2 materials were studied in photodegradation reactions of tartrazine yellow dye. **Figure 8** shows the UV-Vis absorption spectrum (300 to 800 nm) of tartrazine yellow dye with a maximum absorption band at 426 nm. This band is attributed to the absorption of π electrons existing in the Azo group (-N = N-) [35,36], belonging to the chemical structure of the dye, as highlighted in **Figure 8**. **Figure 8b** presents the photodegradation experiments considering this 426 nm wavelength and reacting the tartrazine yellow dye with light (gray), SiO_2 (black), and Fe_3O_4/SiO_2-Np (red). The percentage of degradation of the tartrazine yellow dye by light was 10% in 120 min due to the photolysis of light [16,37]. In the photodegradation experiments with SiO_2, we directly added 0.5 g L^{-1} of SiO_2 to the tartrazine yellow dye solution. The same procedure is performed for the Fe_3O_4/SiO_2-Np. Thus, when exposing the tartrazine yellow dye solution to UV light and SiO_2, the percentage of degradation reached only 19% in 120 min. However, the percentage of degradation in the Fe_3O_4/SiO_2-Np was two times higher, reaching 45% in 120 min. These analyses enabled us to establish a mechanism of action of these materials. For SiO_2, most of the photogenerated electrons in the CB quickly encounter the holes in the VB, resulting in few radicals to degrade tartrazine yellow dye [38]. In contrast, Fe_3O_4/SiO_2-Np presents mixed regions called heterojunctions. These heterojunctions [8,9] alter the quantum efficiency to inhibit recombination between electrons and holes, increasing the quantity of charges in the material that generate the $O_2^{\bullet -}$ and $HO^{\bullet}$ radicals [9,39]. Thus, the degradation efficiency of the tartrazine yellow dye increased from 19% with SiO_2 to 45% with the Fe_3O_4/SiO_2-Np. The lower-than-expected efficiency in photodegradation may be attributed to the geometrical polymorphism of the material and the low quantity of heterojunctions between the materials, which cause recombination between electron/hole charges intrinsically. Some studies reported that the formation of composite materials with core@shell structures tends to create numerous heterojunctions, which decreases the band gap, facilitating transitions and charge generation in the catalyst [40,41]. In this work, the synthesis did not generate a core@shell system, which reduced the number of heterojunctions and decreased the degradation efficiency. However, this rapid and simple synthesis is still advantageous for large-scale application in the decontamination of effluents composed of organic compounds since the synthesis

reuses a biomass commonly discarded and with low-cost chlorides, and the material is magnetically reusable.

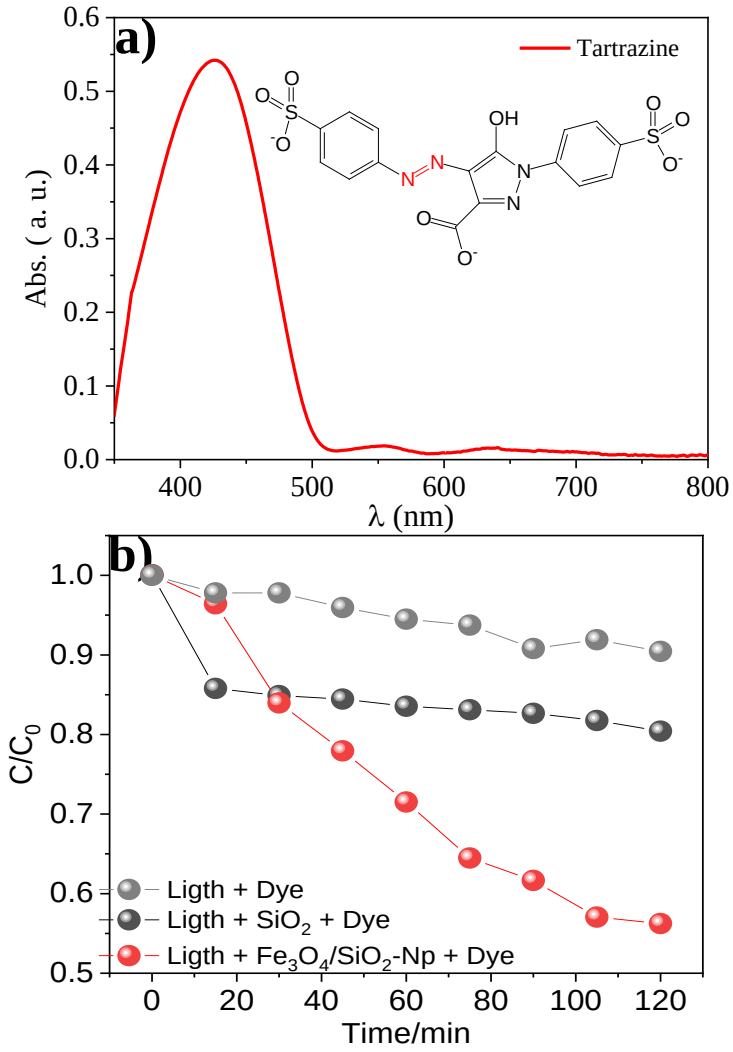

Figure 8. (a) UV-Vis adsorption spectrum of tartrazine yellow dye highlighting its chemical structure; **(b)** tartrazine yellow dye concentration as a function of photodegradation time to photolysis (gray), SiO_2 (black), and Fe_3O_4/SiO_2-Np (red).

4. Conclusion

The use of biomass from sugarcane bagasse was successfully used as a precursor material for silica with crystallinity. This material was a support for the synthesis of Fe_3O_4 nanoparticles. It generated some heterojunctions that increased the efficiency of photodegradation of tartrazine yellow dye. In a rapid, simple, and inexpensive synthesis route, the mixed material using polymeric nano- and microparticles resulted in a 45% degradation percentage of the tartrazine yellow dye in 120 min of reaction time. This implies that this material can act in aqueous systems in the decontamination of dyes containing the azo group. This easy and fast synthesis of the Fe_3O_4/SiO_2 nanocomposite meets the objective of a versatile and efficient material in the degradation of organic dyes, compared to other materials that present complex, expensive, and time-consuming configurations to obtain for the same purpose.

Author contributions: Analyses and experiments, NST and PVRB; interpreting, MVAM and JPdCO; writing, MVAM and JPdCO; discussing the results, MVAM and JPdCO. All authors have read and agreed to the published version of the manuscript.

Acknowledgments: The authors are grateful for the master's degree scholarship from Coordenação de Aperfeiçoamento de Pessoal de Nível Superior (CAPES) and Multidisciplinary Laboratory of Nanomaterials/UFCAT, coordinated by Maria Rita de Cássia Santos, for the support.

Conflict of interest: The authors declare no conflict of interest.

References

1. Fernandes J, Ramísio PJ, Puga H. A Comprehensive Review on Various Phases of Wastewater Technologies: Trends and Future Perspectives. Eng. 2024; 5(4): 2633-2661. doi: 10.3390/eng5040138
2. Saim AK, Adu PCO, Amankwah RK, et al. Review of catalytic activities of biosynthesized metallic nanoparticles in wastewater treatment. Environmental Technology Reviews. 2021; 10(1): 111-130. doi: 10.1080/21622515.2021.1893831
3. Saravanan A, Deivayanai VC, Kumar PS, et al. A detailed review on advanced oxidation process in treatment of wastewater: Mechanism, challenges and future outlook. Chemosphere. 2022; 308: 136524. doi: 10.1016/j.chemosphere.2022.136524
4. Saeed M, Muneer M, Haq A ul, et al. Photocatalysis: an effective tool for photodegradation of dyes—a review. Environmental Science and Pollution Research. 2021; 29(1): 293-311. doi: 10.1007/s11356-021-16389-7
5. Qumar U, Hassan JZ, Bhatti RA, et al. Photocatalysis vs adsorption by metal oxide nanoparticles. Journal of Materials Science & Technology. 2022; 131: 122-166. doi: 10.1016/j.jmst.2022.05.020
6. Ibrahim NS, Leaw WL, Mohamad D, et al. A critical review of metal-doped TiO2 and its structure–physical properties–photocatalytic activity relationship in hydrogen production. International Journal of Hydrogen Energy. 2020; 45(53): 28553-28565. doi: 10.1016/j.ijhydene.2020.07.233
7. Medhi R, Marquez MD, Lee TR. Visible-Light-Active Doped Metal Oxide Nanoparticles: Review of their Synthesis, Properties, and Applications. ACS Applied Nano Materials. 2020; 3(7): 6156-6185. doi: 10.1021/acsanm.0c01035
8. Cao Y, Yuan G, Guo Y, et al. Facile synthesis of TiO2/g-C3N4 nanosheet heterojunctions for efficient photocatalytic degradation of tartrazine under simulated sunlight. Applied Surface Science. 2022; 600: 154169. doi: 10.1016/j.apsusc.2022.154169
9. Balu S, Venkatesvaran H, Wang CC, et al. Synthesis of Sulfonic Acid-Functionalized g-C3N4/BiOI Bifunctional Heterojunction for Enhanced Photocatalytic Removal of Tartrazine and PEC Oxygen Evolution Reaction. Inorganics. 2024; 12(9): 243. doi: 10.3390/inorganics12090243
10. Ashiegbu DC, Potgieter HJ. ZnO-based heterojunction catalysts for the photocatalytic degradation of methyl orange dye. Heliyon. 2023; 9(10): e20674. doi: 10.1016/j.heliyon.2023.e20674
11. Shahzad K, Jamshaid M, Mustafa AEZMA, et al. Synergistic silver-titania nano-composites: Optimized hetero-junction for enhanced water decontamination. Desalination and Water Treatment. 2024; 320: 100696. doi: 10.1016/j.dwt.2024.100696
12. Thambiliyagodage C. Activity enhanced TiO2 nanomaterials for photodegradation of dyes—A review. Environmental Nanotechnology, Monitoring & Management. 2021; 16: 100592. doi: 10.1016/j.enmm.2021.100592
13. Liu S, Yu B, Wang S, et al. Preparation, surface functionalization and application of Fe3O4 magnetic nanoparticles. Advances in Colloid and Interface Science. 2020; 281: 102165. doi: 10.1016/j.cis.2020.102165
14. Lee J, Son N, Shin H, et al. An eco-efficient dual-function technology: Magnetically recoverable rGO-WO3/Fe3O4 ternary heterojunction catalytic system simultaneously performing malachite green photolysis and Cr(VI) reduction. Journal of Cleaner Production. 2024; 459: 142533. doi: 10.1016/j.jclepro.2024.142533
15. Liu M, Ye Y, Ye J, et al. Recent Advances of Magnetite (Fe3O4)-Based Magnetic Materials in Catalytic Applications. Magnetochemistry. 2023; 9(4): 110. doi: 10.3390/magnetochemistry9040110
16. Martins M, Santos TM, Faria EA, et al. Synthesis, Characterization and Application of Magnetic Nanoparticles for the Photodegradation of Tartrazine Yellow Dye. Revista Virtual de Química. 2024; 16(5): 740-747. doi: 10.21577/1984-6835.20240038

17. Ponce J, Andrade JG da S, dos Santos LN, et al. Alkali pretreated sugarcane bagasse, rice husk and corn husk wastes as lignocellulosic biosorbents for dyes. Carbohydrate Polymer Technologies and Applications. 2021; 2: 100061. doi: 10.1016/j.carpta.2021.100061
18. Alarcón E, Hernández C, García G, et al. Changes in chemical and structural composition of sugarcane bagasse caused by alkaline pretreatments [Ca(OH)2 and NaOH] modify the amount of endoglucanase and β-glucosidase produced by Aspergillus niger in solid-state fermentation. Chemical Engineering Communications. 2021; 209(5): 594-606. doi: 10.1080/00986445.2021.1881777
19. Morán-Aguilar MG, Calderón-Santoyo M, de Souza Oliveira RP, et al. Deconstructing sugarcane bagasse lignocellulose by acid-based deep eutectic solvents to enhance enzymatic digestibility. Carbohydrate Polymers. 2022; 298: 120097. doi: 10.1016/j.carbpol.2022.120097
20. Rao S, Madhushree M, Bhat KS. Characteristics of surface modified sugarcane bagasse cellulose: application of esterification and oxidation reactions. Scientific Reports. 2024; 14(1). doi: 10.1038/s41598-024-75846-8
21. Zhou F, Li K, Hang F, et al. Efficient removal of methylene blue by activated hydrochar prepared by hydrothermal carbonization and NaOH activation of sugarcane bagasse and phosphoric acid. RSC Advances. 2022; 12(3): 1885-1896. doi: 10.1039/d1ra08325b
22. Melesse GT, Hone FG, Mekonnen MA. Extraction of Cellulose from Sugarcane Bagasse Optimization and Characterization. Advances in Materials Science and Engineering. 2022; 2022: 1-10. doi: 10.1155/2022/1712207
23. Prabhath N, Kumara BS, Vithanage V, et al. A Review on the Optimization of the Mechanical Properties of Sugarcane-Bagasse-Ash-Integrated Concretes. Journal of Composites Science. 2022; 6(10): 283. doi: 10.3390/jcs6100283
24. Zafeer Mohd K, Menezes RA, Venkatachalam H, et al. Sugarcane bagasse-based biochar and its potential applications: a review. Emergent Materials. 2023; 7(1): 133-161. doi: 10.1007/s42247-023-00603-y
25. Bortolotto Teixeira L, Guzi de Moraes E, Paolinelli Shinhe G, et al. Obtaining Biogenic Silica from Sugarcane Bagasse and Leaf Ash. Waste and Biomass Valorization. 2020; 12(6): 3205-3221. doi: 10.1007/s12649-020-01230-y
26. Seroka NS, Taziwa R, Khotseng L. Green Synthesis of Crystalline Silica from Sugarcane Bagasse Ash: Physico-Chemical Properties. Nanomaterials. 2022; 12(13): 2184. doi: 10.3390/nano12132184
27. Rasheed HA, Adeleke AA, Nzerem P, et al. Isolation, characterization and response surface method optimization of cellulose from hybridized agricultural wastes. Scientific Reports. 2024; 14(1). doi: 10.1038/s41598-024-65229-4
28. Churam T, Usubharatana P, Phungrassami H. Sustainable Production of Carboxymethyl Cellulose: A Biopolymer Alternative from Sugarcane (Saccharum officinarum L.) Leaves. Sustainability. 2024; 16(6): 2352. doi: 10.3390/su16062352
29. Gutierrez FV, Lima IS, De Falco A, et al. The effect of temperature on the synthesis of magnetite nanoparticles by the coprecipitation method. Heliyon. 2024; 10(4): e25781. doi: 10.1016/j.heliyon.2024.e25781
30. Khatun R, Mamun MSA, Islam S, et al. Phytochemical-Assisted Synthesis of Fe3O4 Nanoparticles and Evaluation of Their Catalytic Activity. Micromachines. 2022; 13(12): 2077. doi: 10.3390/mi13122077
31. Haryński Ł, Olejnik A, Grochowska K, et al. A facile method for Tauc exponent and corresponding electronic transitions determination in semiconductors directly from UV–Vis spectroscopy data. Optical Materials. 2022; 127: 112205. doi: 10.1016/j.optmat.2022.112205
32. Narzary S, Alamelu K, Raja V, et al. Visible light active, magnetically retrievable Fe3O4@SiO2@g-C3N4/TiO2 nanocomposite as efficient photocatalyst for removal of dye pollutants. Journal of Environmental Chemical Engineering. 2020; 8(5): 104373. doi: 10.1016/j.jece.2020.104373
33. Rukhsar M, Ahmad Z, Rauf A, et al. An Overview of Iron Oxide (Fe3O4) Nanoparticles: From Synthetic Strategies, Characterization to Antibacterial and Anticancer Applications. Crystals. 2022; 12(12): 1809. doi: 10.3390/cryst12121809
34. Kumar R, Sakthivel R, Behura R, et al. Synthesis of magnetite nanoparticles from mineral waste. Journal of Alloys and Compounds. 2015; 645: 398-404. doi: 10.1016/j.jallcom.2015.05.089
35. Hegazy AA, Haliem WA, Haliem RA, et al. Brief Overview about Tartrazine Effects on Health. European Chemical Bulletin. 2023; 12(1): 4698-4707.
36. Leulescu M, Rotaru A, Pălărie I, et al. Tartrazine: physical, thermal and biophysical properties of the most widely employed synthetic yellow food-colouring azo dye. Journal of Thermal Analysis and Calorimetry. 2018; 134(1): 209-231. doi: 10.1007/s10973-018-7663-3
37. Paiu M, Favier L, Lutic D, et al. Visible-Light Photocatalytic Degradation of Tartrazine Using ZnO Nanoparticles: Preliminary Phytotoxicity Investigations on Treated Solutions. Zenodo. 2024. doi: 10.5281/ZENODO.11145258

38. Bouarroudj T, Aoudjit L, Djahida L, et al. Photodegradation of tartrazine dye favored by natural sunlight on pure and (Ce, Ag) co-doped ZnO catalysts. Water Science and Technology. 2021; 83(9): 2118-2134. doi: 10.2166/wst.2021.106
39. Prasanna SB, Kumar GS, Sakthivel R, et al. Dual Z-scheme heterojunction Ce2Sn2O7/Ag3PO4/V@g-C3N4 for increased photocatalytic degradation of the food additive tartrazine, in the presence of persulfate: Kinetics, toxicity, and density functional theory studies. Environmental Pollution. 2024; 356: 124196. doi: 10.1016/j.envpol.2024.124196
40. Jabbar ZH, Ebrahim SE. Synthesis, characterization, and photocatalytic degradation activity of core/shell magnetic nanocomposites (Fe3O4@SiO2@Ag2WO4@Ag2S) under visible light irradiation. Optical Materials. 2021; 122: 111818. doi: 10.1016/j.optmat.2021.111818
41. Khoshnam M, Salimijazi H. Synthesis and characterization of magnetic-photocatalytic Fe3O4/SiO2/a-Fe2O3 nano core-shell. Surfaces and Interfaces. 2021; 26: 101322. doi: 10.1016/j.surfin.2021.101322